

Application of Particle Image Velocimetry and Reference Image Topography to jet shock cells using the hydraulic analogy

Vaibhav Kumar · Ivan Ng · Gregory J. Sheard ·
Eric Brocher · Kerry Hourigan · Andreas Fouras

Received: 20 August 2010 / Revised: 28 February 2011 / Accepted: 10 March 2011 / Published online: 24 March 2011
© Springer-Verlag 2011

Abstract This paper examines the shock cell structure, vorticity and velocity field at the exit of an underexpanded jet nozzle using a hydraulic analogy and the Reference Image Topography technique. Understanding the flow in this region is important for the mitigation of screech, an aeroacoustic problem harmful to aircraft structures. Experiments are conducted on a water table, allowing detailed quantitative investigation of this important flow regime at a greatly reduced expense. Conventional Particle Image Velocimetry is employed to determine the velocity and vorticity fields of the nozzle exit region. Applying Reference Image Topography, the wavy water surface is reconstructed and when combined with the hydraulic analogy, provides a pressure map of the region. With this approach subtraction of surfaces is used to highlight the unsteady regions of the flow, which is not as convenient or quantitative with conventional Schlieren techniques. This allows a detailed analysis of the shock cell structures and their interaction with flow instabilities in the shear layer that are the underlying cause of jet screech.

1 Introduction

The flow behind jet nozzles has been of great interest due to its effects on the aerodynamics, propulsion and structure of aircraft. The first shock cells at the exit of an underexpanded jet nozzle provide valuable information regarding

the flow properties, including pressure variations, exhaust velocity, acoustic waves and viscous effects. A thorough understanding of the velocity flow field and pressure distribution at the nozzle exit can assist in various studies, such as the investigation of screech phenomena (Brocher and Makhssud 1997; Buchanan et al. 2007) and reduction in shear layer turbulence levels (Alkislar et al. 2003, 2007). Underexpansion is more common with high speed aircraft at high altitudes, where the ambient atmospheric pressure is low, making the flow at the exhaust capable of further expansion. Screech, as an aeroacoustic phenomenon commonly found in underexpanded jets, is potentially harmful for aircraft as it can cause sonic fatigue failure. While a complete understanding of the phenomenon has remained elusive, it is commonly understood that the process responsible for screech generation includes the growth of hydrodynamic instabilities in the shear layer of a shock-containing jet, their interaction with shock cell structures in the core and the subsequent formation of a resonant feedback mechanism that involves the radiation of acoustic waves upstream towards the nozzle exit (Brocher and Makhssud 1997; Buchanan et al. 2007; Chatterjee et al. 2009; Panda 1998; Powell 1953a, b; Raman 1997, 1999; Singh and Chatterjee 2007). Dominant discrete screech tones traveling in the upstream direction are capable of causing structural damage and fatigue failure (Panda 1998). It is therefore essential to understand the flow regime more precisely to develop appropriate control mechanisms for screech.

Schlieren photography in wind tunnels has remained the dominant technique to visualize flow and measure screech since the seminal research of Powell (1953a, b). Schlieren photography visualizes density variations in a fluid, thus allowing the imaging of shock waves with great clarity. While it is a relatively low cost technique with high sensitivity, it is largely a qualitative visualization process.

V. Kumar · I. Ng · G. J. Sheard · K. Hourigan · A. Fouras (✉)
Division of Biological Engineering, Faculty of Engineering,
Monash University, Clayton, VIC 3800, Australia
e-mail: andreas.fouras@monash.edu

E. Brocher
Institut de Mécanique des Fluides de Trets, Trets 13530, France

Various other methods have been adopted for the measurement of velocity and pressure fields in a two-dimensional flow, but they have been characterized by either probes intruding and disrupting the flow, pressure distribution being derived from the velocity flow field and thus dependent on the accurate measurement of velocity, or experiment being complicated or expensive to set up (Jaw et al. 2009; Kuroda and Ogawa 1987).

While air flow has previously been analogized to two-dimensional water flow on a water table with a hydraulic analogy (Black and Mediratta 1951; Brocher and Makhssud 1997; Buchanan et al. 2007; Rani and Wooldridge 2000), the visualization technique has again remained predominantly Schlieren with probes used to measure acoustic frequencies. The purpose of this study is to demonstrate the applicability of a novel non-obtrusive optical method with the hydraulic analogy to map the pressure distribution and velocity at the nozzle exit. The fundamental approach employed in this study is Particle Image Velocimetry (PIV), in which two subsequent images are compared to calculate the instantaneous displacement and velocity. This study utilizes the high sensitivity of refraction-based visualization methods (Jähne et al. 1994) and combines the Reference Image Topography technique (Fouras et al. 2006; Fouras et al. 2008b) with the hydraulic analogy to enable detailed quantitative analysis of the flow behind an underexpanded jet, a flow region which has been of concern to many researchers (Alkislar et al. 2003, 2007; Brocher and Makhssud 1997; Buchanan et al. 2007).

2 The hydraulic analogy

According to the hydraulic analogy, the free-surface topography of shallow water relates to the pressure, temperature and density profiles of the flow, while the velocity field is directly related to the vorticity (Buchanan et al. 2007; Fouras et al. 2008b).

The similarity between the wave patterns produced by a supersonic body in air and surface waves produced by a moving ship was first observed by Mach (1887). Jouguet (1920) and Riabouchinsky (1932) developed the relationship between two-dimensional gas flow and free-surface water flow into an analogy which could be used for practical purposes.

The hydraulic analogy is useful for simulating high-speed two-dimensional compressible ideal gas flow with shallow water flow (Brocher and Makhssud 1997; Buchanan et al. 2007). The study of high-speed jet flows becomes much more simple, convenient and accurate, as the wave propagation and flow speed are three orders of magnitude slower than gas flow. Differences in pressure, temperature and density in gas flow correspond to differences in water depth

across a converging nozzle placed on the water table. The Froude number, Fr , in the water is considered analogous to the Mach number, Ma , for gas flow (Buchanan et al. 2007), subsequently allowing pressure ratios across the nozzle to determine the equivalent speed of the gas (White 1999). Dynamic equivalence between the two flows is achieved by a simple manipulation of equations (as in Eqs. 1, 2), i.e.,

$$Ma \equiv Fr = \left[2 \left(\frac{h}{h_0} - 1 \right) \right]^{1/2} \dots \gamma = 2, \quad (1)$$

$$R = \frac{p}{p_0} = \left[1 + \frac{1}{2}(\gamma - 1)Ma^2 \right]^{\gamma/(\gamma-1)} \dots \gamma = 2, \quad (2)$$

where γ is the specific heat ratio, h and p are the water depth and pressure, respectively, in the upstream reservoir, h_0 and p_0 are the mean water depth and mean pressure, respectively, in the test section, and R is the equivalent pressure ratio. A highly detailed mathematical analysis of the analogy was presented by Preiswerk (1938), which is summarized concisely in Table 1.

It is worth noting that the analogy does not provide a direct quantitative representation of aerodynamic flows in air, but rather that of a hydraulic gas in which γ is 2 (Black and Mediratta 1951). However, this restriction can be neglected as most relevant experiments, including in this study, are not significantly influenced by varying γ (Brocher and Makhssud 1997).

Powell (1953a) noted that the wavelength of the standing waves is highly dependent on the pressure ratio of the jet. The critical water depth ratio, for which the Froude number in the hydraulic analogy is unity at the nozzle exit, is equal to 1.5. Thus the corresponding critical pressure ratio for the hydraulic gas is $1.5^2 = 2.25$ (Brocher and Makhssud 1997).

3 Water table design

A water table provides a convenient experimental apparatus for applying the hydraulic analogy to study high-speed

Table 1 Analogous equations and variables for shallow hydraulic flow and 2D flow of a compressible gas

Gas flow	Hydraulic flow	Implication
$\frac{T}{T_0} = 1 + \frac{\gamma-1}{2} Ma^2$	$\frac{h}{h_0} = 1 + \frac{1}{2} Fr^2$	$\frac{T}{T_0} \equiv \frac{h}{h_0}; \gamma = 2$
$\frac{\partial}{\partial x} (\rho u) + \frac{\partial}{\partial y} (\rho v) = 0$	$\frac{\partial}{\partial x} (hu) + \frac{\partial}{\partial y} (hv) = 0$	$Ma \equiv Fr; \frac{\rho}{\rho_0} \equiv \frac{h}{h_0}$
$\frac{p}{p_0} = \frac{\rho}{\rho_0} \frac{T}{T_0}$		$\frac{p}{p_0} = \left(\frac{h}{h_0} \right)^2$

T , h , ρ , and p are the temperature, water depth, density and pressure, respectively, where the symbols with the subscript 0 refer to the mean values and symbols with no subscript refer to the local values. u and v are the axial and lateral fluid velocities, respectively (Buchanan et al. 2007; Preiswerk 1938)

flows. Various studies (Black and Mediratta 1951; Brocher and Makhsood 1997; Buchanan et al. 2007; Giordano and Fleeter 1992; Rani and Wooldridge 2000; Rao et al. 1983; Solomon 1967) have analyzed the free-surface flow on a water table for determining equivalent characteristics of gas flow. Some of the main design features of the water table used in the present study are discussed below.

The water table, identical to that used by Buchanan et al. (2007), was designed based on a similar table used by Brocher and Makhsood (1997). A large horizontal sheet of clear glass (2,000 mm long, 1,410 mm wide and 16 mm thick) constitutes the bed of the water table and its main working section. This flat, transparent glass allows the visualization of flow and/or its illumination from below the table. Appropriate structural support is installed to ensure the local deflection due to gravity does not exceed 0.1 mm, in order to maintain the flatness of the table bed essential for high accuracy of results. The glass bed is bound on its sides by glass walls 95 mm high, thus theoretically allowing water depths of up to 95 mm across the test section.

Water is injected into a supply reservoir upstream of the test section through a thick layer (approximately 100 mm) of small pebbles, so as to minimize the scale of turbulence from pump vibrations and the inflow of water. An alternative to the pebbles is to use wire mesh screens (Black and Mediratta 1951; Rani and Wooldridge 2000; Solomon 1967), but pebbles were considered to be more effective in eliminating large turbulent eddies or a mean transverse flow within the reservoir. A perspex nozzle (described later) separates the upstream and downstream sections of the table. The downstream water depth is adjusted by a metal weir at the end of the working section, the angle of which can be adjusted by its supporting screws. The total length of the weir is 400 mm and its end is rounded with a 5 mm radius curve to allow a smooth flow of water into the downstream reservoir. Each reservoir has a capacity of approximately 500 l. The water level in the downstream reservoir is maintained so as to minimize the development of bubbles from the water falling off the weir into the reservoir.

Water is recycled from the downstream reservoir to the upstream reservoir by a small 1.5 kW centrifugal pump driven by a 2 kW AC motor, with the speed controlled by a variable frequency drive. A feedback control system employs a magnetohydrodynamic flowmeter to provide continuous monitoring of the pump volumetric flow rate output, thereby maintaining a constant flow into the upstream reservoir. The level of the water in the upstream reservoir effectively determines the volumetric flow rate through the nozzle and test section. However the Froude number, as seen from the hydraulic analogy, is a function of the water level ratio and is therefore independent of the

actual volumetric flow rate. The pump output can be adjusted to control this water level. This feedback-control system of the pump allows consistent and repeatable experimental conditions.

In order to counter artificial slowing down of the flow due to viscous drag from the glass bed, the water table is provided a decline of 0.1° with the help of a hydraulic jack incorporated in the design of the table. Foam rubber with triangular cutouts is placed along the side walls of the test section to absorb any transversely propagating waves and prevent reflection from the side walls. The water was regularly filtered to remove any unwanted particles that can affect the PIV process.

3.1 Nozzle design

The perspex nozzle design was based on the ‘N1’ nozzle used by Brocher and Makhsood (1997), with the height of the walls being 80 mm. The same nozzle was used by Buchanan et al. (2007) in their Schlieren study of jet screech. The nozzle consists of parallel walls 135 mm apart, extending for a length of 90 mm, followed by converging walls with a half-angle of 5° for a length of 441 mm. The nozzle exit width is 57 mm, with the nozzle exit lip thickness tapered to approximately 1.5 mm. The small lip thickness prevents amplification of the screech-wave-generation process (Norum 1983; Ponton and Seiner 1992).

As with the slope provided to the working section to reduce drag, the nozzle was designed to provide a secondary, much slower, flow known as co-flow to decrease the mean resistance further and allow for a straighter flow with minimum low frequency noise. The co-flow was generated by drilling holes of approximately 20 mm diameter in the upstream wall on both sides of the nozzle. The amount of co-flow was controlled by covering the number of holes required and smoothed by placing steel wool behind the holes. While the effect of co-flow on the pressure ratio is not completely understood, the presence of co-flow suggests there would be minor differences with Brocher and Makhsood (1997), where there was no co-flow, between the R values at which screech is expected.

4 Flow visualization

4.1 Surface reconstruction

The technique used in this study is based on the Reference Image Topography technique described in Fouras et al. (2006). Shallow water flows at a steady rate through the nozzle placed on the water table. A reference object, attached to the glass bed in the nozzle exit region, is

imaged by a camera from above through still water which is used as a reference image. A light source (300 W halogen lamp), collimated by a long aspect ratio box lined with a reflective surface, is used to illuminate the semi-translucent reference object from below. As the water flows through the nozzle, the disturbed surface distorts the image (Fig. 1). The camera's frame of view encompasses the entire first few shock cells. Comparing the reference image with the distorted image using PIV techniques (Fouras et al. 2008a), a grid of apparent displacement vectors is produced. With appropriate analysis using the height estimation algorithm (described later), these vectors can be used to reconstruct the topography of the distorted surface. Inherently, this is a simple, cost-efficient, highly accurate and easily repeatable visualization technique (Fouras et al. 2006).

The reference object may be attached above or below the glass bed, with the difference in results being negligible for the system used (Moisy et al. 2009). A ground glass plate is used below the water table bed as a reference object, or a 90 μm thick A4 transparency with a high resolution random pattern is used above the bed. A light-diffusing sheet attached below the bed complements the transparency. Images of the ground glass or random pattern resemble those of a dense set of particles, the positions of which are compared using PIV (Fouras et al. 2008a).

A qualitative study using the same technique was conducted earlier by Ng et al. (2010). The schematic of the water table for surface reconstruction is shown in Fig. 2.

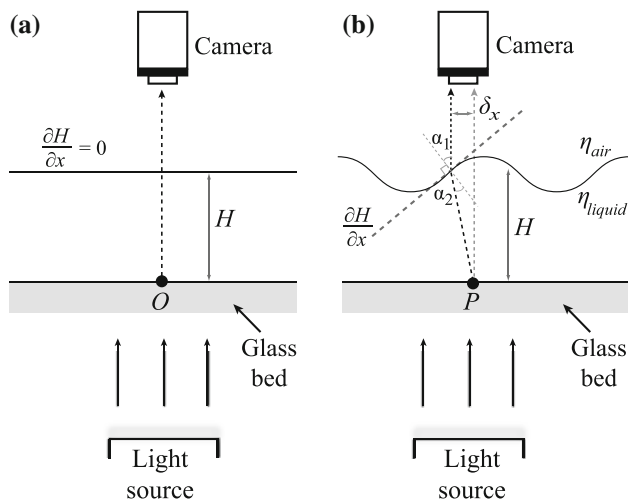


Fig. 1 Geometry and nomenclature for the height estimation algorithm. **a** Undistorted position of point O through an undisturbed surface, **b** Apparent displacement δ_x of point P due to refraction through the surface at height H with gradient $\partial H/\partial x$. Refractive indices of the air η_{air} and liquid η_{liquid} phases are shown, as are the refraction angles α_1 and α_2 [adapted from Ng et al. (2011)]

4.2 Height estimation algorithm

The apparent displacement vectors (δ_x , δ_y) relate to the free-surface gradients ($\partial H/\partial x$ and $\partial H/\partial y$), which can be integrated by an algorithm to estimate the water depth distribution, or the height above the glass bed (Fouras et al. 2008b). The mean water height, set as the reference height (H_{ref}), is taken as the initial height estimate, H . Based on the configuration in Fig. 1 and using Snell's law of refraction at the water-air interface ($\eta_{\text{air}} \sin \alpha_1 = \eta_{\text{liquid}} \sin \alpha_2$), the relationship to estimate $\partial H/\partial x$ and $\partial H/\partial y$ using the current guesses of H was derived in Fouras et al. (2008b) as

$$\tan^{-1} \frac{\delta_x}{H} = \tan^{-1} \frac{\partial H}{\partial x} - \sin^{-1} \left[\frac{\eta_{\text{air}}}{\eta_{\text{liquid}}} \sin \left(\tan^{-1} \frac{\partial H}{\partial x} \right) \right], \quad (3)$$

Integrating $\partial H/\partial x$ and $\partial H/\partial y$ yields the estimated heights, which can be adjusted to give H_{adj} by applying a minimum-error approach between measured displacements and reference image particle positions. An iterative process is applied until the value of H_{adj} converges. A detailed description of the height-solving algorithm is contained in Fouras et al. (2008b).

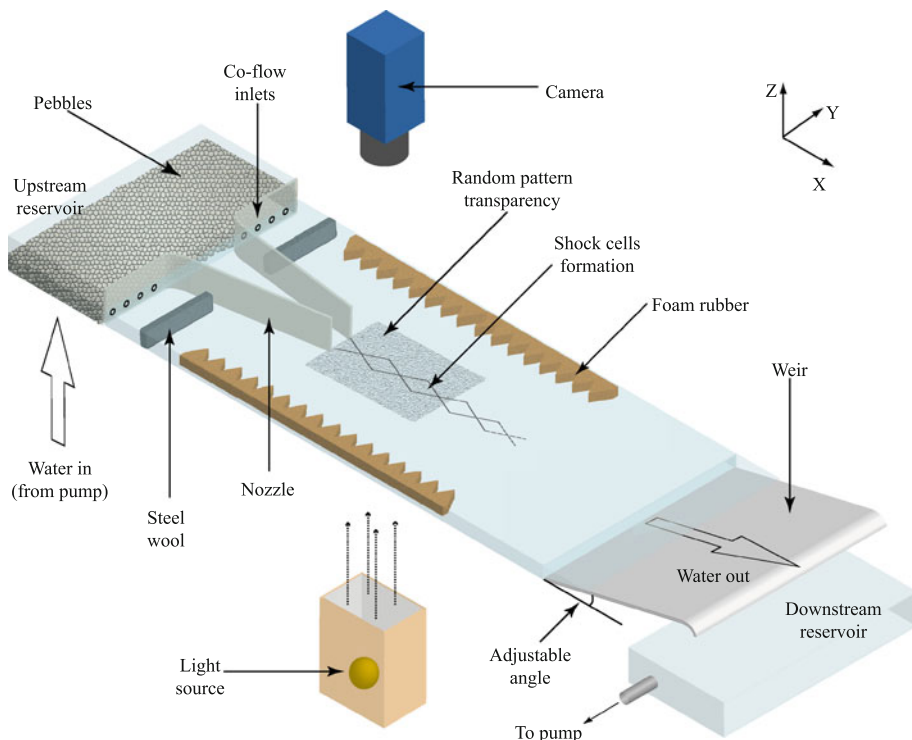
4.3 Velocity

The velocity field of the flow is determined using conventional PIV techniques, where tracer particles are seeded in the flow and their motion used to indirectly measure the fluid flow (Fouras et al. 2008a; Raffel et al. 2007). The particles, chosen to be of similar density to the fluid, are assumed to faithfully follow the flow dynamics, giving a highly accurate representation. A balance was required for the particles to be big enough to allow a good scatter of incident laser light for PIV, while being small enough so as to not sink prematurely on the glass bed. Twenty six micrometer polystyrene particles provided the optimal size in this study.

A high-speed camera (MotionPro Y6) was installed below the water table immediately after imaging from the top, to image the velocity of the same flow. This sequential process was followed due to the restriction of the diffuser and reference object otherwise obstructing the view from below. The same field of view was imaged by the top and bottom cameras. Particles were illuminated by a horizontal laser sheet through the water (Nd:YAG, $\lambda = 532$ nm) and images were recorded at 500 Hz.

The pressure and velocity fields can be measured simultaneously by imaging a horizontal laser sheet through seeded water, eliminating the need for a reference object. This method was applied by Ng et al. (2011) by installing a twin-camera system, with one camera imaging the laser sheet from below the water table while the other focuses on

Fig. 2 Schematic of the water table and placement of camera and nozzle. Water flows from the upstream reservoir through the perspex nozzle to form a shock cell pattern above a certain equivalent pressure ratio. The shock cell pattern distorts the image of the random pattern transparency, illuminated from below, and captured by the camera above the table for PIV analysis. The angle of the weir is adjustable to maintain the water depth required in the test section. Steel wool smooths the co-flow and foam rubber triangular cutouts absorb waves, preventing reflection back into the imaged region. A pump is used to recycle water upstream from the downstream reservoir



the same plane from above. This provides the added benefit of allowing temporal analysis of the topography and velocity together. It also results in greater accuracy due to simultaneous measurements, though making the system slightly more sensitive with the same frame of view on the laser sheet being imaged by two cameras.

5 Results

The upstream water depth was varied to control the pressure ratio and hence the resulting Mach number (as per Eq. 1). A low downstream water depth was chosen to produce well-defined shock cells with relatively low surface gradients for effective height estimation. An interrogation window size of 16 pixels \times 16 pixels was chosen to provide high accuracy and effective vector correlation, given the field-of-view size and particle size.

5.1 Time-averaged measurements

The time-averaged surface reconstruction, velocity and vorticity profiles for $R = 3.1$ shock cells are shown in Fig. 3. The harmonics are clearly evident in the reconstruction, with greater pressure gradients visible at the shock cell corners. The first shock cell at the nozzle's exit is especially distinct with sharp gradients. The initial top-hat velocity distribution of the jet gradually relaxes to an asymptotic bell-shaped velocity profile downstream.

The vorticity profile [calculated using the method described by Fouras and Soria (1998)] indicates a laminar flow upstream, with flow becoming turbulent in the shear region downstream. The flat areas in the surface correspond to regions where fluctuations in the surface average out, whereas the shock cells are visible because they are clearly defined structures which are fixed in place in the actual flow. Decay in the strength of the shock cells can be observed with distance downstream.

5.2 Time-resolved measurements

The time-averaged surface (Fig. 3) is subtracted from the instantaneous surfaces to emphasize the time-dependent features of the flow. This is depicted in Fig. 4 for a lower pressure ratio, where periodic vortices propagate downstream on either side of the shock cells. The presence of vortices is inferred from the low pressure regions of the pressure maps, as vorticity is not directly calculated from these maps. The vortex structures are thus represented by the periodic surface instabilities in the shear layer. Over time, these vortices are averaged to the mean water depth, as exhibited by the flat regions in Fig. 3. It is hypothesized that these vortex structures pump fluid into and out of the jet shear layer (Woodmansee et al. 2004). Panda (1999) and Alkislar et al. (2003) observed the movement of these structures using Schlieren visualization. However, by completely reconstructing the fluid motion, the technique presented in this paper provides clarity and scope for more

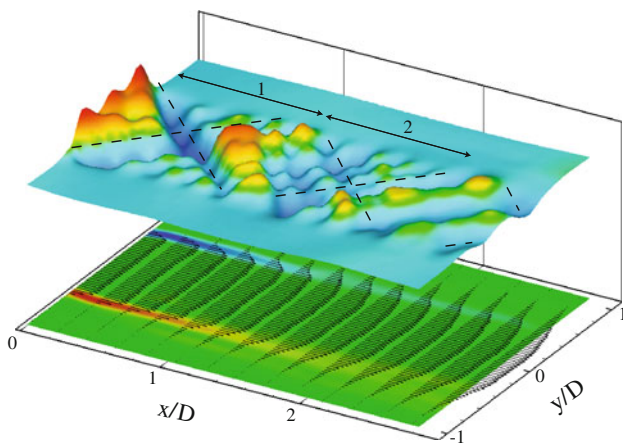


Fig. 3 Time-averaged surface reconstruction of the shock cells (top) and vorticity and velocity distribution (bottom) for $R = 3.1$. The variation in water surface in the region of the first two shock cells is distinct. The jet shear layer region (either side of the shock cells) can be seen to be averaged out to the mean water depth over time. The vorticity is seen to gradually spread downstream, while the velocity distribution (shown by the vectors) gradually relaxes from a top-hat to an asymptotic bell-shaped velocity profile. The camera's frame of view is 2.842 units (x/D) \times 2.132 units (y/D) = 1,504 pixels streamwise \times 1,128 pixels lateral, with the nozzle exit at the origin of the coordinate system

detailed qualitative and quantitative analysis. Subtraction of images, for example, becomes a useful tool with Reference Image Topography.

These vortex structures originate from Kelvin-Helmholtz instabilities caused by the shear in the streamwise direction in the expanding jet (Chandrasekhar 1961; Drazin 1970). The vortices can be seen to originate from the shear layer outside the first shock cell and the vorticity increases in strength downstream. This is verified in Fig. 5, where it can be seen that in general the intensity of the vortices increases further downstream, at least up to the 4th or 5th shock cell in view. The sharp increase in mean vortex intensity at the end of the second shock cell is consistent with the significance of the local pressure gradient established in this region by Brocher and Makhssud (1997). The plot reflects the root mean square of the difference from the mean water depth along the axial distance, averaged over 500 data points in sequence (approximately 35 s). Interaction between the larger vortices and shock cells downstream produces instabilities in the jet core region, which can be linked to the generation of acoustic power at the screech frequency (Buchanan et al. 2007). The strength of these vortices is purported to be related to the screech-tone intensity (Alkislar et al. 2003). The aeroacoustic phenomenon of screech, being potentially harmful for aircraft bodies, is an area of continual research and investigation (Alkislar et al. 2003; Buchanan et al. 2007; Chatterjee et al. 2009; Kurbatskii 2010; Liu et al. 2009; Menshov et al. 2009; Raman 1999; Singh and Chatterjee 2007).

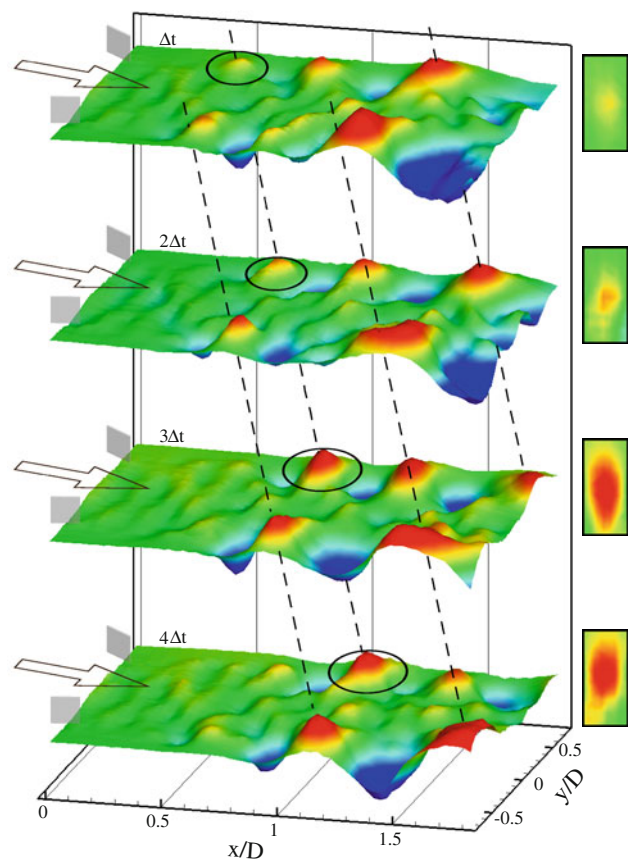


Fig. 4 A time sequence of fluctuations subtracted from the time-averaged surface topography, highlighting the steady propagation and growth of instabilities in the shear layer for a lower pressure ratio. $\Delta t = 0.44$ screech cycles and flow is from left to right. The surface topography represents a pressure map of the nozzle exit region, with the red and blue colors signifying high and low pressures, respectively. The top-down views in the corresponding insets of the circled structures verify the increase in size and strength of the structure. The relatively flat iso-surface in the vicinity of the nozzle exit shows that the pressure field is relatively time independent in this region

The velocity of vortex propagation is found by generating a figure of the pressure mapped on axes of downstream position versus time (see Fig. 5a). The gradient of the parallel diagonal lines provides a measure of the average velocity of vortex propagation. For the flow in Fig. 4, the corresponding gradients are calculated from Fig. 5a to be approximately 7.2 mm/s.

It can be seen from Fig. 5 that the number of vortices upstream is significantly greater than downstream. The number of vortices are observed to increase in strength while decreasing in frequency downstream as a result of a period-doubling phenomenon. This is consistent with previous observations that waves grow, merge and distort to form large-scale coherent vortex structures (Alkislar et al. 2003, 2007; Ho and Huang 1982; Morris et al. 1990; Zhang et al. 2009).

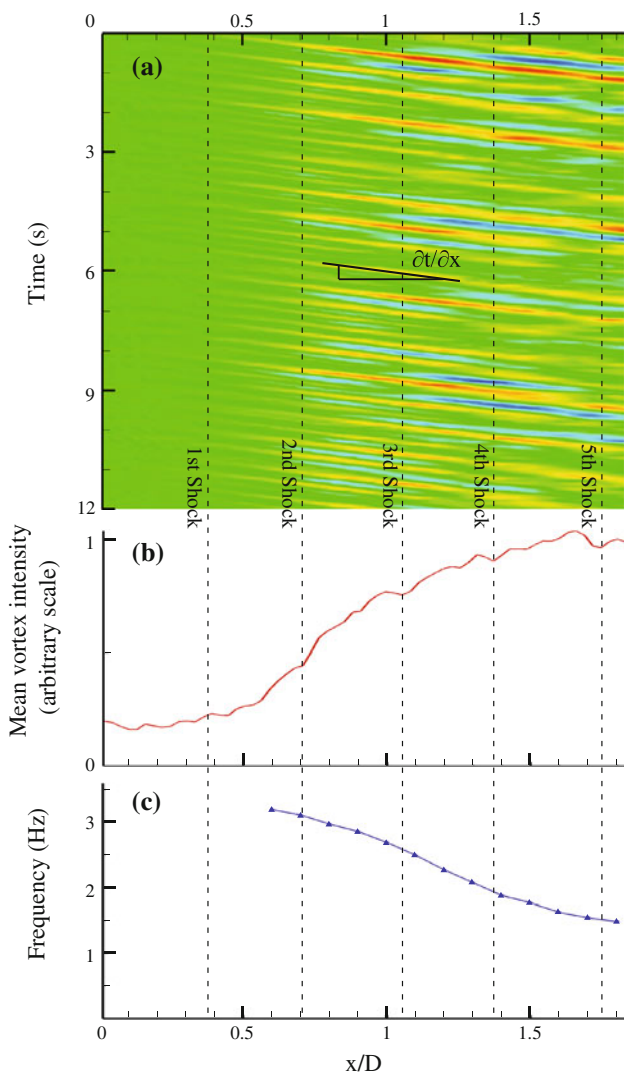


Fig. 5 **a** Propagation of vortices with time, **b** intensity variation and **c** frequency of vortex propagation for a lower pressure ratio. The red and blue colors in (**a**) signify the variation in water depth from the mean water depth. Vertical lines represent the positions of the first five shocks. The instability begins to form after approximately the first shock and gains in strength from the second shock onwards, as shown in plot (**b**). The gradient of the diagonal lines is used to determine the average velocity of the vortex, calculated here to be approximately 7.2 mm/s. The instabilities from upstream merge and distort to form larger, more intense, coherent structures downstream, resulting in period-doubling as confirmed in plot (**c**)

5.3 Pressure variation of instability

Figure 6a traces a particular low pressure feature (a diagonal line in Fig. 5), showing a gradual increase in the average pressure of the vortex center. The shock positions are represented by the vertical lines. From Figs. 5 and 6a it is evident that the instability is measurable after the first shock and gains rapidly in strength only after the second shock. Figure 6b shows the gradient of this hydrodynamic fluctuation plotted against axial position. It is interesting to

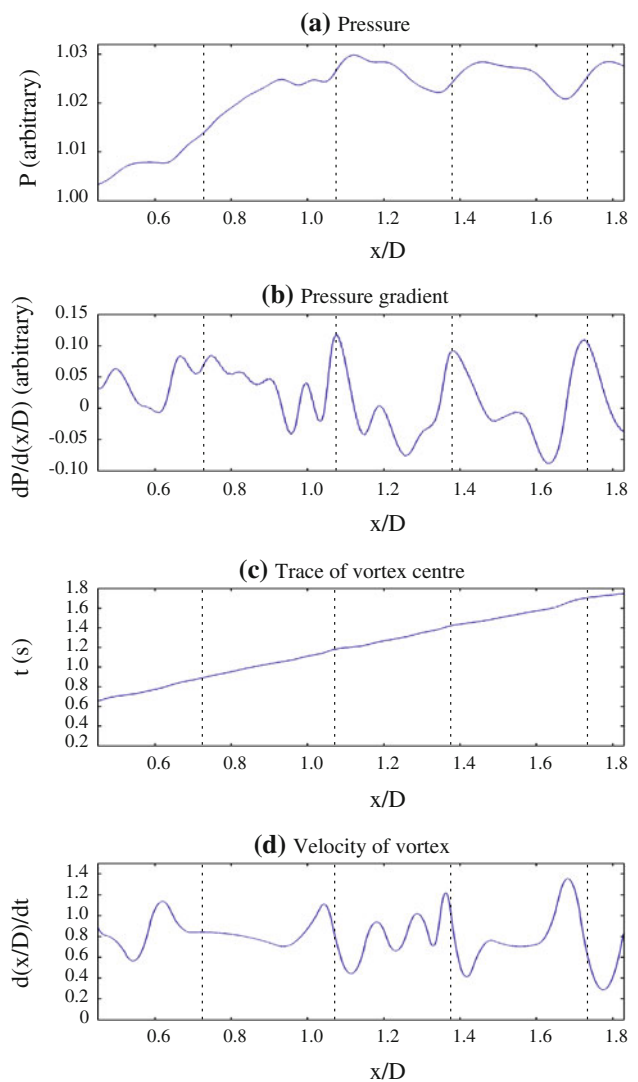


Fig. 6 **a** Pressure variation for a single vortex structure with flow downstream (left to right). Pressure is standardized with mean pressure level. The vertical lines represent the positions of the 2nd, 3rd, 4th and 5th shocks. **b** Spatial derivative of the pressure variation, **c** Position of vortex center with time, and **d** Vortex velocity. The positions of the shocks appear to correspond closely to the local maxima of plot (**b**), indicating a sudden surge in pressure increase at the shocks. Sudden decreases in velocity (plot (**d**)) are evident at the shocks, suggesting that the acoustic noise source is in the vicinity of shocks

note that the pressure tends to increase much faster in regions near shocks. The pressure variation is much stronger after the second shock, when the shear layer instabilities start interacting with the shock cells in the jet core. This also corresponds to the sudden increases and decreases in vortex velocity seen around the shocks (Fig. 6c, d). These high pressure and velocity gradients at the end of the shock cells are closely associated with the generation of screech (Alkislar et al. 2003), especially at the end of the second cell for the hydraulic analogy (Brocher and Makhsud 1997).

The techniques described herein could also be used to determine the sources of sound, such as jet screech, in supersonic jets and predict the acoustic pressure levels.

The acoustic wave equation for an isentropic flow is given by Powell (1964) as

$$\frac{1}{c_0^2} \frac{\partial^2 p'}{\partial t^2} - \frac{\partial^2 p'}{\partial x_i^2} = \nabla \cdot \left[\rho(\boldsymbol{\omega} \times \mathbf{v}) + \nabla \left(\frac{1}{2} \rho |\mathbf{v}|^2 \right) - \mathbf{v} \frac{\partial \rho}{\partial t} - \frac{1}{2} |\mathbf{v}|^2 \nabla \rho \right]. \quad (4)$$

The right hand side of the above equation are the acoustic source terms: Particle Image Velocimetry can be used to determine the velocity and vorticity fields, and the density field is obtained from the hydraulic analogy using Reference Image Topography. A numerical mesh can be set up, as per Liow et al. (2006), and the source terms can then be calculated at each node. The acoustic wave equation can then be solved numerically to determine the far field wave propagation and the flow structures responsible for generating these waves.

Qualitatively, a rapid acceleration and deceleration of the jet shear layer vortices is seen in Fig. 6d as they encounter a pressure drop and then a sharp pressure peak at the end of each shock cell. For each vortex, the source terms in the above equation can change rapidly due to this change in velocity and pressure, thereby generating acoustic radiation; the first term is the incompressible source term leading to “vortex sound”. A feedback loop is then set up, as described by Powell (1964), whereby the incipient jet shear layer is most receptive to this acoustic radiation, leading to vortex waves (and the formation of vortices) in the shear layer which then interact with the shock cell pressure gradients to complete the loop.

As the region observed here is close to the jet boundary, the hydrodynamic fluctuations dominate the pressure field, confirming previous observations (Brocher and Makhsud 1997; Panda 1999; Singh and Chatterjee 2007). Further away from the jet core laterally, we would expect to see acoustic noise contributions. That region has not been imaged primarily due to limitations with the frame-of-view used.

6 Conclusions

Combining the well-established Particle Image Velocimetry technique with Reference Image Topography and the hydraulic analogy on a water table has provided a unique insight into compressible flow dynamics. The combination of these optical techniques with a low-cost experimental set-up allows for detailed analyses which are more convenient, simpler, less expensive and more accurate than

other visualization methods. The application of PIV to surface refraction physics through Reference Image Topography allows the entire reconstruction of the water surface. Combining this with the hydraulic analogy generates a pressure map, which when studied with the velocity and vorticity fields, allows in-depth quantitative understanding of the flow.

The flow behind a jet nozzle has been examined in this study, which can be further investigated for developing screech mitigation measures. The qualitative as well as quantitative data from the experiments conducted are comparable to those from supersonic wind tunnels, albeit at a significantly lower cost. The shear layer instabilities, shock cell structures and their interactions have been quantitatively visualized with high resolution in the nozzle exit region. There is potential to measure the velocity and pressure distributions simultaneously by using a twin-camera system, one from above and one from below the water table, to image a laser sheet through seeded water.

References

- Alkislar MB, Krothapalli A, Lourenco LM (2003) Structure of a screeching rectangular jet: a stereoscopic particle image velocimetry study. *J Fluid Mech* 489:121–154
- Alkislar MB, Krothapalli A, Butler GW (2007) The effect of streamwise vortices on the aeroacoustics of a Mach 0.9 jet. *J Fluid Mech* 578:139–169. doi:[10.1017/S0022112007005022](https://doi.org/10.1017/S0022112007005022)
- Black J, Mediratta OP (1951) Supersonic flow investigation with a “hydraulic analogy” water channel. *Aeronaut Q* 2:227–253
- Brocher E, Makhsud A (1997) A new look at the screech tone mechanism of underexpanded jets. *Eur J Mech B/Fluids* 16(6):877–891
- Buchanan A, Macartney R, Thompson MC, Brocher E, Hourigan K (2007) Hydraulic analogy study of supersonic rectangular-jet screech control with cylinders. *AIAA J* 45(7):1539–1545. doi:[10.2514/1.26714](https://doi.org/10.2514/1.26714)
- Chandrasekhar S (1961) Hydrodynamic and hydromagnetic stability. Clarendon Press, Oxford
- Chatterjee A, Ghodake D, Singh A (2009) Screech frequency prediction in underexpanded axisymmetric screeching jets. *Int J Aeroacoust* 8(5):499–510. doi:[10.1260/147547209788549307](https://doi.org/10.1260/147547209788549307)
- Drazin PG (1970) Kelvin-Helmholtz instability of finite amplitude. *J Fluid Mech* 42(2):321–335. doi:[10.1017/S0022112070001295](https://doi.org/10.1017/S0022112070001295)
- Fouras A, Soria J (1998) Accuracy of out-of-plane vorticity measurements derived from in-plane velocity field data. *Exp Fluids* 25(5–6):409–430. doi:[10.1007/s003480050248](https://doi.org/10.1007/s003480050248)
- Fouras A, Hourigan K, Kawahashi M, Hirahara H (2006) An improved, free surface, topographic technique. *J Vis* 9(1):49–56
- Fouras A, Lo Jacono D, Hourigan K (2008) Target-free stereo PIV: a novel technique with inherent error estimation and improved accuracy. *Exp Fluids* 44(2):317–329. doi:[10.1007/s00348-007-0404-1](https://doi.org/10.1007/s00348-007-0404-1)
- Fouras A, Lo Jacono D, Sheard GJ, Hourigan K (2008) Measurement of instantaneous velocity and surface topography in the wake of a cylinder at low Reynolds number. *J Fluids Struct* 24(8):1271–1277

- Giordano DD, Fleeter S (1992) Investigation of oscillating airfoil shock phenomena. *J Phys III* 2(4):595–612
- Ho C, Huang L (1982) Subharmonics and vortex merging in mixing layers. *J Fluid Mech* 119:443–473. doi:[10.1017/S002211208008842](https://doi.org/10.1017/S002211208008842)
- Jähne B, Klinke J, Waas S (1994) Imaging of short ocean wind waves: a critical theoretical review. *J Opt Soc Am A* 11(8):2197–2209. doi:[10.1364/JOSAA.11.002197](https://doi.org/10.1364/JOSAA.11.002197)
- Jaw SY, Chen JH, Wu PC (2009) Measurement of pressure distribution from PIV experiments. *J Vis* 12(1):27–35. doi:[10.1007/BF03181940](https://doi.org/10.1007/BF03181940)
- Jouguet E (1920) Some problems in general hydrodynamics. *J Math Pures Appl* (Series 8) 31
- Kurbatskii KA (2010) Numerical simulation of axisymmetric jet screech tones using a general purpose finite-volume CFD code. In: 48th AIAA aerospace sciences meeting including the new horizons forum and aerospace exposition, Orlando, Florida
- Kuroda C, Ogawa K (1987) Static pressure-velocity field in a turbulent jet. *AIChE J* 33(3):519–523. doi:[10.1002/aic.690330322](https://doi.org/10.1002/aic.690330322)
- Liow YSK, Tan BT, Thompson MC, Hourigan K (2006) Sound generated in laminar flow past a two-dimensional rectangular cylinder. *J Sound Vib* 295(1–2):407–427. doi:[10.1016/j.jsv.2006.01.014](https://doi.org/10.1016/j.jsv.2006.01.014)
- Liu J, Kailasanath K, Ramamurti R, Munday D, Gutmark E, Lohner R (2009) Large-eddy simulations of a supersonic jet and its near-field acoustic properties. *AIAA J* 47(8):1849–1865. doi:[10.2514/1.43281](https://doi.org/10.2514/1.43281)
- Mach E (1887) Photography of projectile phenomena in air. *Sitzungberichte der Wiener Akademie* 95:164
- Menshov I, Semenov I, Ahmedyanov I, Ibrahim MK, Nakamura Y (2009) Towards understanding the physics of supersonic jet screech. In: Choi H, Choi HG, Yoo JY (eds) Computational fluid dynamics 2008. Springer, Berlin, pp 101–106 doi:[10.1007/978-3-642-01273-0](https://doi.org/10.1007/978-3-642-01273-0)
- Moisy F, Rabaud M, Salsac K (2009) A synthetic schlieren method for the measurement of the topography of a liquid interface. *Exp Fluids* 46(6):1021–1036. doi:[10.1007/s00348-008-0608-z](https://doi.org/10.1007/s00348-008-0608-z)
- Morris PJ, Giridharan MG, Lilley GM (1990) On the turbulent mixing of compressible free shear layers. *Proc Roy Soc Lond A* 431:219–243. doi:[10.1098/rspa.1990.0128](https://doi.org/10.1098/rspa.1990.0128)
- Ng I, Kumar V, Sheard GJ, Hourigan K, Fouras A (2010) Surface topography of jet shock cells in a hydraulic analogy. *J Vis* 13(3):175–176. doi:[10.1007/s12650-010-0032-3](https://doi.org/10.1007/s12650-010-0032-3)
- Ng I, Kumar V, Sheard GJ, Hourigan K, Fouras A (2011) Experimental study of simultaneous measurement of velocity and surface topography: In the wake of a circular cylinder at low Reynolds number. *Exp Fluids* 50(3):587–595. doi:[10.1007/s00348-010-0960-7](https://doi.org/10.1007/s00348-010-0960-7)
- Norum TD (1983) Screech suppression in supersonic jets. *AIAA J* 21(2):235–240
- Panda J (1998) Shock oscillation in underexpanded screeching jets. *J Fluid Mech* 363:173–198. doi:[10.1017/S0022112098008842](https://doi.org/10.1017/S0022112098008842)
- Panda J (1999) An experimental investigation of screech noise generation. *J Fluid Mech* 378:71–96. doi:[10.1017/S0022112098003383](https://doi.org/10.1017/S0022112098003383)
- Ponton MK, Seiner JM (1992) The effects of nozzle exit lip thickness on plume resonance. *J Sound Vib* 154(3):531–549
- Powell A (1953) On the mechanism of choked jet noise. *Proc Phys Soc Lond B* 66:1039–1056
- Powell A (1953) On the noise emanating from a two-dimensional jet above critical pressure. *Aeronaut Q* 4(2):103–122
- Powell A (1964) Theory of vortex sound. *J Acoust Soc Am* 36(1):177–195
- Preiswerk E (1938) Application of the methods of gas dynamics to water flows with free surface. Tech. rep., Mitteilungen der Institut für Aerodynamik, No. 7, E.T.H. Zurich, translated as N.A.C.A. T.N. 934
- Raffel M, Willert CE, Wereley ST, Kompenhans J (2007) Particle Image Velocimetry—a practical guide, 2nd edn. Springer, Berlin
- Raman G (1997) Cessation of screech in underexpanded jets. *J Fluid Mech* 336:69–90. doi:[10.1017/S002211209600451X](https://doi.org/10.1017/S002211209600451X)
- Raman G (1999) Supersonic jet screech: Half-century from Powell to the present. *J Sound Vib* 225(3):543–571. doi:[10.1006/jsvi.1999.2181](https://doi.org/10.1006/jsvi.1999.2181)
- Rani SL, Wooldridge MS (2000) Quantitative flow visualization using the hydraulic analogy. *Exp Fluids* 28(2):165–169
- Rao JS, Rao VVR, Seshadri V (1983) Hydraulic analogy for isentropic flow through a nozzle. *Def Sci J* 33(2):97–111
- Riabouchinsky D (1932) On the hydraulic analogy to flow of a compressible fluid. *Comptes Rendus de l'Academie des Sciences* 195(22):998
- Singh A, Chatterjee A (2007) Numerical prediction of supersonic jet screech frequency. *Shock Waves* 17(4):263–272. doi:[10.1007/s00193-007-0110-1](https://doi.org/10.1007/s00193-007-0110-1)
- Solomon L (1967) A hydraulic analogue study of the Hartmann oscillator phenomenon. *J Fluid Mech* 28(2):261–271
- White FM (1999) Fluid mechanics, 4th edn. McGraw-Hill, Singapore
- Woodmansee MA, Iyer V, Dutton JC, Lucht RP (2004) Nonintrusive pressure and temperature measurements in an underexpanded sonic jet flowfield. *AIAA J* 42(6):1170–1180. doi:[10.2514/1.10418](https://doi.org/10.2514/1.10418)
- Zhang J, Liu N, Lu X (2009) Route to a chaotic state in fluid flow past an inclined flat plate. *Phys Rev E* 79(4):045,306. doi:[10.1103/PhysRevE.79.045306](https://doi.org/10.1103/PhysRevE.79.045306)